

# Large anomalous Nernst and inverse spin-Hall effects in epitaxial thin films of Kagome semimetal Mn<sub>3</sub>Ge

Deshun Hong<sup>1</sup>, Naween Anand<sup>1</sup>, Changjiang Liu<sup>1</sup>, Haihua Liu<sup>2</sup>, Ilke Arslan<sup>2</sup>, John E. Pearson<sup>1</sup>, Anand Bhattacharya<sup>1</sup> and J. S. Jiang<sup>1\*</sup>

<sup>1</sup>*Materials Science Division, Argonne National Laboratory, Argonne, Illinois 60439, USA;*

<sup>2</sup>*Center for Nanoscale Materials, Argonne National Laboratory, Argonne, Illinois 60439, USA;*

Fabrication of crystallographically well-defined thin films of topological materials is important for unraveling their mesoscale quantum properties and for device applications. Mn<sub>3</sub>Ge, an antiferromagnetic Weyl semimetal with a chiral spin texture on a Kagome lattice, is expected to have enhanced Berry curvature around Weyl nodes near the Fermi energy, leading to large anomalous Hall / Nernst effects and spin-Hall effect in transport. Using magnetron sputtering, we have grown epitaxial thin films of hexagonal D0<sub>19</sub> Mn<sub>3</sub>Ge that are highly crystalline, flat and continuous. Large anomalous Nernst and inverse spin-Hall effects are observed in thermoelectric and spin pumping devices. The anomalous Nernst coefficient in the Mn<sub>3</sub>Ge films is estimated to be 0.1  $\mu\text{V}/\text{K}$ , and is comparable to that of Fe, despite Mn<sub>3</sub>Ge having a weak magnetization of  $\sim 0.003 \mu_{\text{B}} / \text{Mn}$  atom. The spin mixing conductance and spin-Hall angle in Mn<sub>3</sub>Ge are estimated to be 3.5 and 7 times of those in Pt, respectively.

The recent discoveries of topological properties in layered Kagome semimetals such as Mn<sub>3</sub>X (X = Sn [1-5], Ge [4-6]), Fe<sub>3</sub>Sn<sub>2</sub> [7, 8] and Co<sub>3</sub>Sn<sub>2</sub>S<sub>2</sub> [9-11] have attracted broad interests in these materials. Due to breaking of time reversal symmetry, spin degeneracy is lifted, and pairs of Weyl nodes are generated in reciprocal space according to glide mirror plane symmetry in Mn<sub>3</sub>X [4]. Giant anomalies in Hall resistance and Nernst coefficient which are comparable with those of ferromagnetic materials have been reported [1, 3]. These anomalies are attributed to the non-zero Berry phase gained around Weyl nodes and the effects are similar to applying fictitious field of  $\sim 100$  T [2, 12]. Theoretical calculations also indicate large spin-Hall angles in these materials [13], which is useful for antiferromagnetic spintronics. Inverse spin-Hall effect [14] as well as large magneto-optical Kerr effect [15] have been measured which has same origin as anomalies in transport.

The hexagonal D0<sub>19</sub> phase of Mn<sub>3</sub>Ge has a layered Kagome structure and is antiferromagnetic with a geometrically frustrated 120° triangular magnetic structure all the way to low temperatures. As a Weyl semimetal, Mn<sub>3</sub>Ge has many more Weyl points near the Fermi surface than the closely related Mn<sub>3</sub>Sn, presumably due to lower spin-orbit coupling. The magnetic structure in Mn<sub>3</sub>Ge is different from that of Mn<sub>3</sub>Sn, and this results in a different mirror symmetry as well as different positions of Weyl nodes in Brillouin zone [4]. Topological properties in Mn<sub>3</sub>Ge has been investigated by transport [6] and most of these works are performed on bulk samples [16]. Thin films offer the possibility of tuning topological phases with strain, proximity effects and gating, and are well suited for exploration of fundamental mesoscopic transport properties and device applications. Therefore, synthesis of crystallographically well-defined Mn<sub>3</sub>Ge thin film is of great interest.

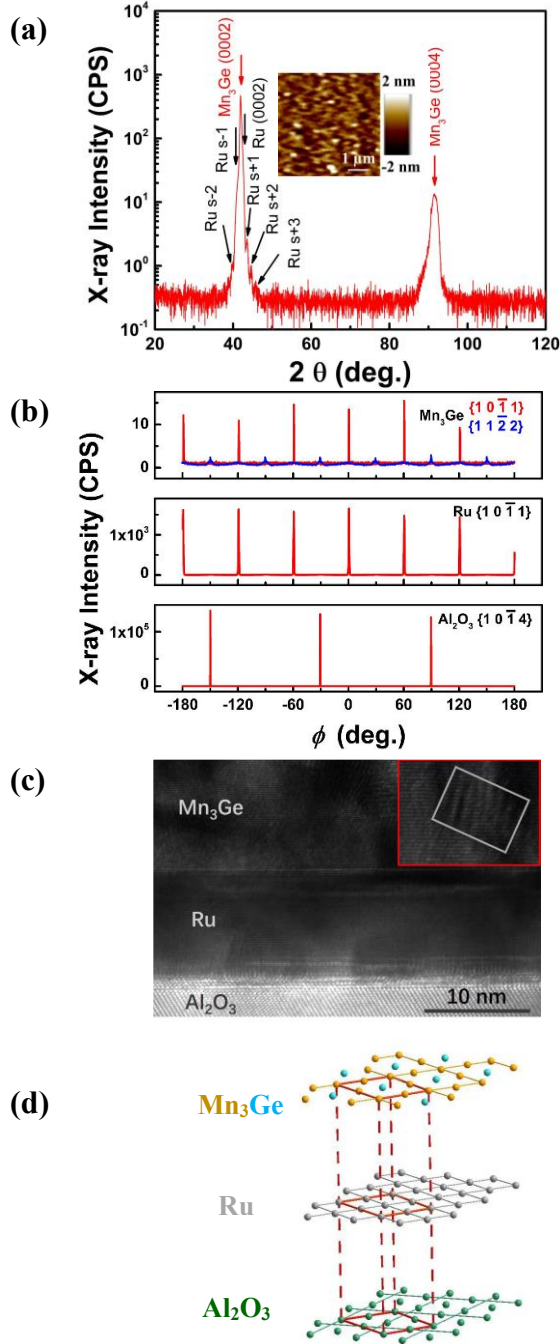


Fig. 1 (a) X-ray diffraction of sputtering grown Mn<sub>3</sub>Ge on Ru-buffered sapphire (0001). Ru satellite peaks are labeled as s followed by their order. Inset: AFM image of the film. (b) Phi scan around partially in-plane peaks (as labeled) of Mn<sub>3</sub>Ge, Ru and substrate correspondingly. (c) TEM image viewing along sapphire [10 $\bar{1}$  0] axis. Inset: Moiré lattice in Mn<sub>3</sub>Ge. (d) Stacking configuration among Mn<sub>3</sub>Ge, Ru and substrate according to phi scan. For simplicity, we choose oxygen termination in sapphire substrate.

Until now, several groups have reported their results on Mn<sub>3</sub>Sn or Mn<sub>3</sub>Ge thin film synthesis [17-20], with polycrystalline structure. In this work, we grow Mn<sub>3</sub>Ge thin films epitaxially on Ru-buffered single-crystal sapphire by magnetron sputtering. X-ray diffraction (XRD) and high-resolution transmission electron microscopy (HRTEM) indicate the formation of hexagonal D0<sub>19</sub> Mn<sub>3</sub>Ge with *c*-axis oriented out-of-plane. By fabricating the Mn<sub>3</sub>Ge films into thermoelectric and spin pumping devices, we observed large anomalous Nernst as well as inverse spin-Hall effects. The anomalous Nernst coefficient in Mn<sub>3</sub>Ge is comparable to that of Fe, despite Mn<sub>3</sub>Ge having a weak magnetization of  $\sim 0.003 \mu_B$  / Mn atom. The spin mixing conductance and spin-Hall angle in Mn<sub>3</sub>Ge are estimated to be 3.5 and 7 times of those in Pt, respectively.

Previous growth of Mn<sub>3</sub>Sn [18] suggest this high surface energy material tends to have wetting issue and is discontinuous after growth. Here, we find that continuous epitaxial Mn<sub>3</sub>Ge films can be successfully grown by magnetron sputtering onto Ru-buffered sapphire (0001) substrate at high rate and lower temperature. Mn and Ge were co-sputtered from elemental sources. Their atomic fluxes were measured in situ using a quartz crystal microbalance (QCM) which had been calibrated using x-ray reflectivity measurements. To determine the optimal growth conditions, we varied the Mn-to-Ge flux ratio and analyzed the composition of the resulting films using Rutherford backscattering spectrometry (RBS). Remarkably, the formation of (0001)-oriented single-phase D0<sub>19</sub> Mn<sub>3</sub>Ge occurred only when the flux ratio was maintained at close to 5.07, indicating a less-than-unity sticking coefficient for the Mn adatom at the growth temperature. Details of the growth are as follows: The Ru buffer layer was deposited at 3.6 nm/min at 350°C, and then annealed at 700°C for 15

minutes. This procedure produced a very flat Ru (0002) surface, as evidenced by sharp streaks in the RHEED patterns and the satellite peaks in high-angle XRD spectra. The Mn<sub>3</sub>Ge layer was subsequently deposited onto the Ru template at 400°C and at an Argon sputter gas pressure of 2.5 mTorr. The effective total deposition rate of the Mn<sub>3</sub>Ge layer was approximately 10 nm/min. After deposition, the films were annealed under vacuum at 500°C for up to 2 hours to improve crystallinity and chemical order. The heating and cooling rates during all stages of growth were 50°C/min and 20°C/min, respectively. The composition of the final films was determined using RBS to be Mn<sub>3.23±0.05</sub>Ge, which is very similar to that of bulk single crystals (Mn<sub>3.22</sub>Ge) where extra Mn is needed to stabilize the D0<sub>19</sub> structure [16].

Fig. 1(a) shows the XRD 2θ-ω scan of a sapphire/Ru(10nm)/ Mn<sub>3</sub>Ge (100nm) sample. We intentionally offset ω by 0.2° from the sapphire (0006) reflection to avoid the strong substrate contribution. Only the Mn<sub>3</sub>Ge (0002) and (0004) peaks and the Ru (0002) and its satellite peaks can be seen in the entire scan range. The position of the Mn<sub>3</sub>Ge (0002) peak gives  $c = 4.308\text{\AA}$ , which is very close to the bulk value of 4.312Å. Furthermore, using the bulk in-plane lattice constant  $a=5.352\text{\AA}$ , we were able to locate the Bragg peaks of Mn<sub>3</sub>Ge {10 $\bar{1}$ 1} and {11 $\bar{2}$ 2} planes at their respective calculated 2θ and χ positions in the azimuthal XRD φ-scans as shown in Fig. 1(b). We therefore conclude that the sputtered Mn<sub>3</sub>Ge films are also fully relaxed. The inset of Fig. 1(a) shows the atomic force microscope (AFM) image of the sample indicating that the sputtered film is continuous and has a rather featureless surface topography, with a root mean square (RMS) roughness of ~ 2.5 nm.

To determine the in-plane orientation of the Mn<sub>3</sub>Ge films and the epitaxial relationship, azimuthal XRD φ-scans were performed for Bragg peaks of the Mn<sub>3</sub>Ge

and Ru layers and the sapphire substrate. Because the in-plane lattice constant  $a$  of Mn<sub>3</sub>Ge is nearly double that of Ru, and the lattice constants  $c$  of Mn<sub>3</sub>Ge and Ru are nearly the same but are close to 1/3 that of sapphire, care was taken to select Bragg peaks that have no other peaks nearby. Shown in Fig. 1(b) are the φ-scans of Mn<sub>3</sub>Ge {10 $\bar{1}$ 1} and {11 $\bar{2}$ 2}, Ru {10 $\bar{1}$ 1}, and sapphire {10 $\bar{1}$ 4} planes taken at their expected 2θ and χ positions. The sapphire {10 $\bar{1}$ 4} planes have a three-fold symmetry, while the Ru basal hexagon is rotated by 30° from that of sapphire. This demonstrates the well-known rotational honeycomb epitaxy between Ru and sapphire [21]. The two φ-scans of Mn<sub>3</sub>Ge show that its basal hexagon is exactly aligned with that of the Ru buffer. However, the peaks in the Mn<sub>3</sub>Ge {11 $\bar{2}$ 2} φ-scan have broader bases, indicating larger mosaicity in those directions. It is worth noting that the intensity ratio of the Mn<sub>3</sub>Ge {10 $\bar{1}$ 1} and {11 $\bar{2}$ 2} peaks is close to the calculated value based on the structure factor [22]. Since atomic disorder in the unit cell leads to deviations from the ideal structure, the agreement between the intensity ratios suggest that there is good atomic ordering in the Mn<sub>3</sub>Ge films.

The crystal quality of the Mn<sub>3</sub>Ge films has been further examined using high resolution transmission electron microscopy (HRTEM). Shown in Fig. 1 (c) is a cross section near the interfaces viewed along the sapphire [10 $\bar{1}$ 0] zone axis. The interface between the Ru and Mn<sub>3</sub>Ge layers is coherent and the Mn<sub>3</sub>Ge layer is well ordered. However, there are Moiré fringes in the HRTEM image that indicate overlapping crystallites with dislocations or different orientations. These crystallites, about 5-10 nm in size, could explain the broadened bases of Mn<sub>3</sub>Ge {11 $\bar{2}$ 2} φ-scan peaks. As will be seen later, defects and grain boundaries also have implications for the reversal of antiferromagnetic domains in the Mn<sub>3</sub>Ge films. In Fig. 1(d) we illustrate the stacking arrangement of the sapphire substrate and

the Ru and Mn<sub>3</sub>Ge layers. For the sapphire lattice, we choose the oxygen layer as termination for simplicity. The epitaxial relationship among them is: sapphire (0001) [10 $\bar{1}$ 0] || Ru (0001) [11 $\bar{2}$ 0] || Mn<sub>3</sub>Ge (0001)[11 $\bar{2}$ 0].

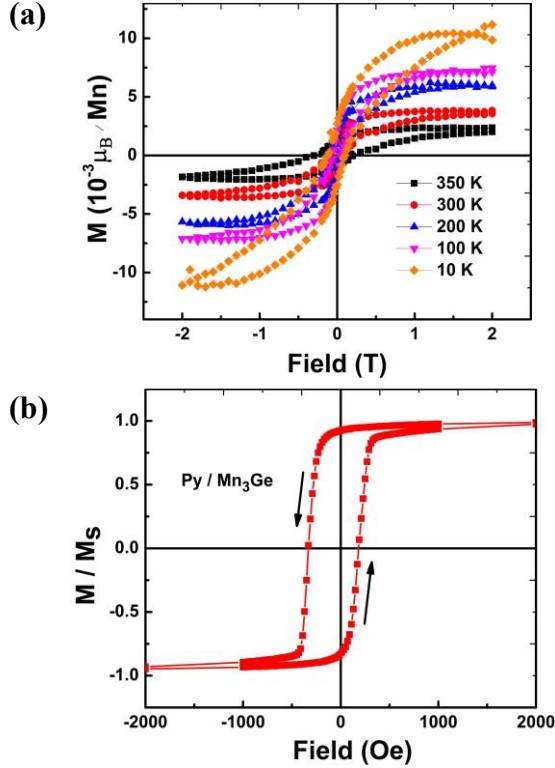


Fig. 2 (a) Field dependences of magnetic moment at various temperatures. Linear diamagnetic backgrounds are subtracted. (b) Field dependence of magnetic moment on Py / Mn<sub>3</sub>Ge / Ru / Sapphire (0001) at 10 K.

Although the hexagonal D0<sub>19</sub> Mn<sub>3</sub>Ge has a triangular antiferromagnetic structure, it possesses a weak in-plane ferromagnetic moment arising from spin canting toward the local easy axis [23]. In bulk Mn<sub>3</sub>Ge single crystals, the ferromagnetic moment amounts to 0.006 - 0.008  $\mu_B$ /Mn at temperatures between 5 and 300 K, and it is noted that this in-plane moment is essential for controlling chirality of the spin structure via applied magnetic field [6, 16]. Shown in Fig. 2(a) is the magnetic field dependence of the in-plane magnetization of a 100 nm Mn<sub>3</sub>Ge film measured at various temperatures using SQUID

magnetometry, after subtracting linear diamagnetic background contribution from substrate. There is a net ferromagnetic moment that increases with decreasing temperature. The ferromagnetic magnetization of the Mn<sub>3</sub>Ge film is  $\sim 0.003 \mu_B / \text{Mn}$  at room temperature, which is close to that of the bulk. The coercive field for switching the ferromagnetic moment is as small as  $\sim 0.06 \text{ T}$  at 300 K and is not very temperature dependent. In Fig. 2 (b), we present the hysteresis loop of a Mn<sub>3</sub>Ge (100nm)/Py(10nm) bilayer structure measured at 10 K after cooling from room temperature in a 1-T in-plane magnetic field. The loop is shifted in the negative field direction by  $\sim 75 \text{ Oe}$ . Given that the triangular spin structure is not expected to have appreciable in-plane magnetic anisotropy, and that the coercivity of the bilayer ( $H_C = 255 \text{ Oe}$ ) is significantly larger than that of a single Py layer (typically less than a few Oe), the occurrence of exchange bias suggests that the antiferromagnetic domains in the Mn<sub>3</sub>Ge layer are pinned, possibly by defects and grain boundaries.

The anomalous Nernst effect (ANE) is a sensitive probe for topological properties in the vicinity of the Fermi energy  $E_F$ . As a counterpart of anomalous Hall effect (AHE), ANE depends only on Berry curvature near the Fermi energy, involving states both above and below  $E_F$  over an extent of energy determined by the broadening of the Fermi function [24]. Due to the particular glide mirror symmetry in the chiral magnetic structures of Mn<sub>3</sub>Ge, the reciprocal space points with non-zero Berry curvature lies in a plane that is perpendicular to the c-axis [6, 12]. The c-axis oriented Mn<sub>3</sub>Ge films are well suited for integration into a thermoelectric device to probe the Berry curvature-driven ANE. On a device shown schematically in Fig.3 (a), we applied an *out-of-plane* thermal gradient via a patterned Au on-chip heater, and an *in-plane* magnetic field perpendicular to the Mn<sub>3</sub>Ge stripe. The ANE signal was detected as a voltage

difference along the length of the Mn<sub>3</sub>Ge stripe at the second harmonic of the excitation of the heater. We corrected for the shunting effect of the Ru buffer layer by employing the parallel-resistor model and the measured electrical resistivities of Ru and Mn<sub>3</sub>Ge. Fig. 3(b) presents the ANE signal  $S_{ij}$  measured at 300 K on a device micro-fabricated from a sapphire/Ru(10nm)/Mn<sub>3</sub>Ge (100nm) sample.

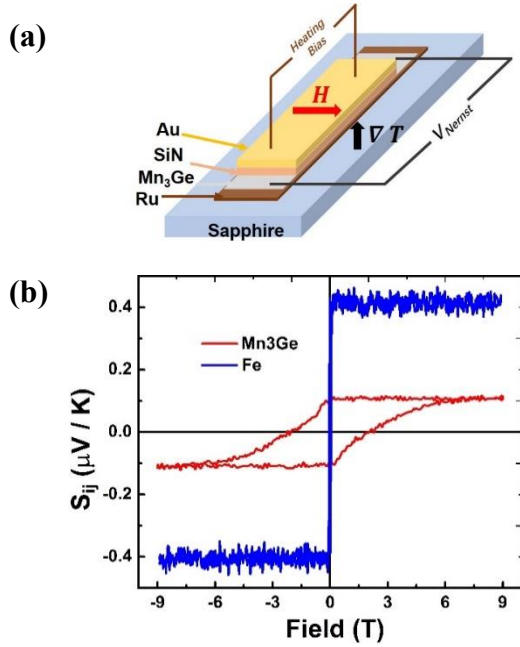


Fig. 3 (a) Schematic of the Nernst device. (b) Nernst signal measured on Mn<sub>3</sub>Ge / Ru / Sapphire and Fe / Sapphire at 300 K

The ANE signal reverses sign when the magnetic field is swept between  $\pm 9$  T and the reversal is hysteretic. Although  $S_{ij}$  starts decreasing as soon as the field polarity is reversed, the sign reversal of  $S_{ij}$  proceeds very slowly and does not complete until the applied field reaches  $\sim 7$  T, giving a coercivity of  $\sim 2$  T. This is significantly greater than the coercivity of 20 to 300 Oe for switching AHE in single crystals Mn<sub>3</sub>Ge [6, 16]. The difference is attributable to the larger number of defects and grain boundaries in the Mn<sub>3</sub>Ge thin films. Although the chiral antiferromagnetic domain in Mn<sub>3</sub>Ge can nucleate reversal easily, the

antiferromagnetic domain walls in thin films could become pinned and increasingly larger fields are then needed to free the domain wall from pinning sites of various strengths. The saturation  $S_{ij} = 0.1 \mu\text{V/K}$  measured in our Mn<sub>3</sub>Ge epitaxial thin film is similar to the  $\sim 0.3 \mu\text{V/K}$  value for that of single-crystal Mn<sub>3</sub>Sn [3], and is also comparable to the  $S_{ij} = 0.4 \mu\text{V/K}$  for Fe measured in an identically micro-fabricated reference device.

Owing to the large spin-Hall conductivity that has been theoretically predicted for Mn<sub>3</sub>Ge [13], a strong spin-to-charge conversion may be expected when a spin current is injected into Mn<sub>3</sub>Ge. We employed ferromagnetic resonance-spin pumping (FMR-SP) to measure the inverse spin-Hall effect (ISHE) in the epitaxial Mn<sub>3</sub>Ge films. The inset of Fig. 4(a) shows a device image and the measurement schematic: On a  $1000\mu\text{m} \times 200\mu\text{m}$  bar of Py/ Mn<sub>3</sub>Ge bilayer film, an electrically-isolated coplanar waveguide (CPW) was patterned along the Mn<sub>3</sub>Ge  $[1\bar{1}00]$  direction and terminated with a 50W resistive load. Microwave excitations with varying frequencies (7 - 18 GHz) and power (12 - 18 dBm) were applied to the CPW to drive magnetization precession in the Py layer. An external magnetic field was applied parallel to the CPW axis and was swept through ferromagnetic resonance. The spin-to-charge conversion due to ISHE was detected. Fig. 4(a) displays the measured  $V_{sp}$  from a Py(10 nm)/Mn<sub>3</sub>Ge (100 nm) device as a function of the applied field, along with the responses from two reference devices identically fabricated from a Py(10 nm)/Pt(10 nm) bilayer and a Py(10 nm) single layer measured under identical conditions.

The measured  $V_{sp}$  is composed of a symmetric component ( $V_{ISHE}$ ) due to the spin pumping-induced ISHE, and an antisymmetric Lorentzian component ( $V_{AHE}$ ) due to the rectified AHE voltage arising from the capacitive coupling-induced rf current and the

magnetization precession in Py [25], along with a constant offset. By fitting the  $V_{sp}$  spectra with symmetric and antisymmetric kernels of the Lorentzian form, we can extract the  $V_{ISHE}$  and  $V_{AHE}$  contributions. Shown in Fig. 4(b) are the ISHE charge current ( $V_{ISHE}/R$ ) for all three devices, where R is the total device resistance across the contact pads. As expected, the Py single layer device is unaffected by ISHE, its  $V_{sp}$  is thus entirely antisymmetric and its  $V_{ISHE}/R$  is negligible. On the other hand, the peak  $V_{ISHE}/R$  value of the Py/Mn<sub>3</sub>Ge device is significantly larger than that of the Py/Pt device. In view of the large variations in the numerical values of parameters related to spin transport and spin-to-charge conversion in the literature [26], we do not attempt to quantify the spin-Hall angle and related parameters for our epitaxial Mn<sub>3</sub>Ge thin films. Instead, a direct comparison between Mn<sub>3</sub>Ge and Pt would be more intuitive.

A gyromagnetic ratio  $\gamma = 1.82 \times 10^{11} T^{-1} s^{-1}$  and saturation magnetization  $\mu_0 M_S = 0.84 T$  for the Py layers in our devices can be obtained by fitting the field dependence of FMR frequency using the Kittel formula and these values are comparable to the work in reference [25]. In the inset of Fig. 4(b), the FMR linewidth ( $\Delta H$ ) as a function of  $f$  is plotted and fitted with the linear relation,  $\Delta H = \left(\frac{2\pi}{\gamma} \alpha_{eff}\right) f + \Delta H_0$  for all devices. This yields Gilbert damping parameters  $\alpha_{eff}$  for the Py, Py/Pt and Py/Mn<sub>3</sub>Ge devices as 0.009, 0.015 and 0.03, respectively. The enhanced damping in the bilayer devices is the result of spin pumping and is related to the spin mixing conductance  $g_r^{\uparrow\downarrow}$  via  $(\alpha_{eff}^{bilayer} - \alpha_{eff}^{Py}) = \left(\frac{\gamma \hbar}{4\pi M_S t_{Py}}\right) g_r^{\uparrow\downarrow}$ . Using the fitted values for  $\alpha_{eff}$ , we obtain  $g_r^{\uparrow\downarrow} = 25.5 \text{ nm}^{-2}$  for the Py/Pt interface, and  $g_r^{\uparrow\downarrow} = 90 \text{ nm}^{-2}$  for Py/Mn<sub>3</sub>Ge.

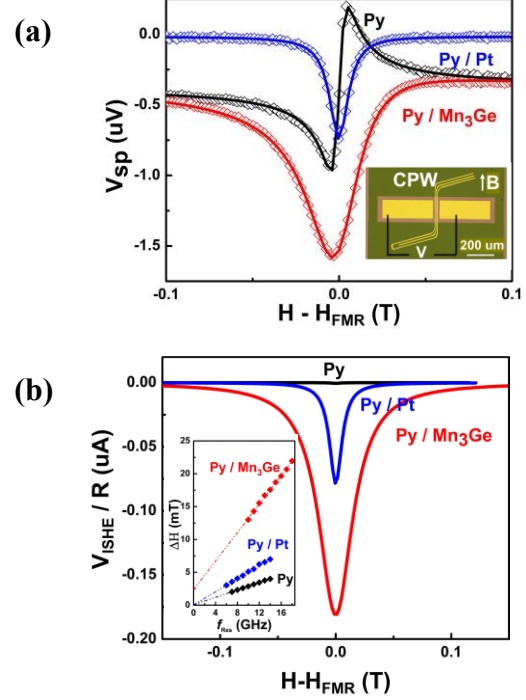


Fig. 4 (a) FMR signal (including both symmetric and anti-symmetric components) measured at 13 GHz and 18 dBm. Solid line is the fitting of the measured data. Inset: Optical image of the spin-pumping device. (b) Inverse spin-Hall signal (symmetric component) measure by FMR. Inset: Linear fit to the resonance linewidth ( $\Delta H$ ) at various resonance frequencies with 18 dBm input power.

In a FMR-SP device, the ISHE voltage depends on the material and device parameters via  $V_{ISHE} = \left(\frac{-e\theta_{SH}}{\sigma_{NM}t_{NM} + \sigma_{FM}t_{FM}}\right) \lambda_{SD} \tanh\left(\frac{t_{NM}}{2\lambda_{SD}}\right) g_r^{\uparrow\downarrow} f L P \left(\frac{\gamma h_{rf}}{2\alpha\omega}\right)^2$  [27] ( $e$  is the electron charge,  $\theta_{SH}$  spin Hall angle,  $\sigma_{NM}$  ( $\sigma_{FM}$ ) is conductivity of NM (FM),  $t_{NM}$  ( $t_{FM}$ ) is thickness of NM (FM),  $L$  is sample length,  $P$  is ellipticity of magnetization precession,  $g_r^{\uparrow\downarrow}$  is mixing conductance). The value of  $h_{rf}$  is unknown in our measurements. However, since our devices are identically fabricated, they are expected to have very similar impedance and thus the  $h_{rf}$  term cancels out when we take the ratio of  $V_{ISHE}$  of devices measured under the same input rf power and frequency. For Py/Pt ( $\lambda_{SD} \approx 3 \text{ nm}$ ,  $\sigma_{NM} \approx 1.0 \times 10^7 (\Omega\text{m})^{-1}$ ) [28] and Py/Mn<sub>3</sub>Ge ( $\lambda_{SD} \approx$

1 nm,  $\sigma_{NM} \approx 3.0 \times 10^5 (\Omega\text{m})^{-1}$ ) [29], the ratio of spin-Hall angles  $\theta_{SH}^{Mn_3Ge}/\theta_{SH}^{Pt}$  is estimated to be around 7. The higher spin-mixing conductivity in the Py/Mn<sub>3</sub>Ge device and the larger spin-Hall angle of Mn<sub>3</sub>Ge are consistent with the theoretical prediction of a large spin-Hall conductivity in Mn<sub>3</sub>Ge.

In summary, we have successfully synthesized continuous epitaxial thin films of the Kagome semimetal Mn<sub>3</sub>Ge by magnetron sputtering. Large anomalous Nernst and inverse spin-Hall effects have been observed in thermoelectric and spin pumping devices fabricated from the Mn<sub>3</sub>Ge thin films. Synthesis of crystallographically well-defined Mn<sub>3</sub>Ge thin films is an important step toward pursuing antiferromagnetic spintronics as well as elucidating the fundamental physics of topological materials.

We acknowledge Dr. Jonathan Gibbons for fruitful discussion in FMR measurement and Dr. Timothy Spila for the acquisition of RBS data. Work at Argonne is supported by the Center for the Advancement of Topological Semimetals, an Energy Frontier Research Center funded by the U.S. DOE, Office of Basic Energy Sciences. The use of facilities at the Center for Nanoscale Materials was supported by the U.S. DOE, BES under Contract No. DE-AC02-06CH11357.

- [1] S. Nakatsuji, N. Kiyohara & T. Higo, *Nature* 527, 212 (2015).
- [2] K. Kuroda, T. Tomita, M. -T. Suzuki, C. Bareille, A. A. Nugroho, P. Goswami, M. Ochi, M. Ikhlas, M. Nakayama, S. Akebi, R. Noguchi, R. Ishii, N. Inami, K. Ono, H. Kumigashira, A. Varykhalov, T. Muro, T. Koretsune, R. Arita, S. Shin, Takeshi Kondo and S. Nakatsuji, *Nat. Mater.* 16, 1090 (2017).
- [3] M. Ikhlas, T. Tomita, T. Koretsune, M. -T. Suzuki, D. N. -Hamane, R. Arita, Y. Otani and S. Nakatsuji, *Nat. Phys.* 13, 1085 (2017).
- [4] H. Yang, Y. Sun, Y. Zhang, W. -J. Shi, S. SP Parkin and B. Yan, *New J. Phys.* 19, 015008 (2017).
- [5] J. Liu and L. Balents, *Phys. Rev. Lett.* 119, 087202 (2017).
- [6] A. K. Nayak, J. E. Fischer, Y. Sun, B. Yan, J. Karel, A. C. Komarek, C. Shekhar, Ni. Kumar, W. Schnelle, J. Kubler, C. Felser and S. S. P. Parkin, *Sci. Adv.* 2, e1501870 (2016).
- [7] L. Ye, M. Kang, J. Liu, F. von Cube, C. R. Wicker, T. Suzuki, C. Jozwiak, A. Bostwick, E. Rotenberg, D. C. Bell, L. Fu, R. Comin, and J. G. Checkelsky, *Nature* 555, 638 (2018).
- [8] J.-X. Yin, S. S. Zhang, H. Li, K. Jiang, G. Chang, B. Zhang, B. Lian, C. Xiang, I. Belopolski, H. Zheng, T. A. Cochran, S.-Y. Xu, G. Bian, K. Liu, T.-R. Chang, H. Lin, Z.-Y. Lu, Z. Wang, S. Jia, W. Wang, and M. Z. Hasan, *Nature* 562, 91 (2018).
- [9] L. Ye, M. K. Chan, R. D. McDonald, D. Graf, M. Kang, J. Liu, T. Suzuki, R. Comin, L. Fu and J. Checkelsky, *Nat. Comm.* 10, 4870 (2019).
- [10] E. Liu, Y. Sun, N. Kumar, L. Muechler, A. Sun, L. Jiao, S. -Y. Yang, D. Liu, A. Liang, Q. Xu, J. Kroder, V. Süß, H. Borrmann, C. Shekhar, Z. Wang, C. Xi, W. Wang, W. Schnelle, S. Wirth, Y. Chen, S. T. B. Goennenwein and C. Felser, *Nat. Phys.* 14, 1125 (2018).
- [11] J. -X. Yin, S. S. Zhang, G. Chang, Q. Wang, S. S. Tsirkin, Z. Guguchia, B. Lian, H. Zhou, K. Jiang, I. Belopolski, N. Shumiya, D. Multer, M. Litskevich, T. A. Cochran, H. Lin, Z. Wang, T. Neupert, S. Jia, H. Lei and M. Z. Hasan, *Nat. Phys.* 15, 443 (2019).
- [12] J. Kübler and C. Felser, *EPL* 120, 47002 (2017).
- [13] Y. Zhang, Y. Sun, H. Yang, J. Zelezny, S. P. P. Parkin, C. Felser and B. Yan, *Phys. Rev. B* 95, 075128 (2017).
- [14] M. Kimata, H. Chen, K. Kondou, S. Sugimoto, P. K. Muduli, M. Ikhlas, Y. Omori, T. Tomita, A. H. MacDonald, S. Nakatsuji and Y. Otani, *Nature* 565, 627 (2019).

- [15] T. Higo, H. Man, D. B. Gopman, L. Wu, T. Koretsune, O. M. J. van't Erve, Y. P. Kabanov, D. Rees, Y. Li, M. -T. Suzuki, S. Patankar, M. Ikhlas, C. L. Chien, R. Arita, R. D. Shull, J. Orenstein and S. Nakatsuji, *Nat. Photon.* 12, 73 (2018).
- [16] N. Kiyohara, T. Tomita, and S. Nakatsuji, *Phys. Rev. Applied* 5, 064009 (2016).
- [17] T. Ogasawara, J. Kim, Y. Ando, A. Hirohata, J. *Magn. Magn. Mater.* 473, 7 (2019).
- [18] A. Markou, J. M. Taylor, A. Kalache, P. Werner, S. S. P. Parkin and C. Felser, *Phys. Rev. Mater.* 2, 051001 (R) (2018).
- [19] T. Higo, D. Qu, Y. Li, C. L. Chien, Y. Otani and S. Nakatsuji, *Appl. Phys. Lett.* 113, 202402 (2018).
- [20] T. Ikeda, M. Tsunoda, M. Oogane, S. Oh, T. Morita and Y. Ando, *Appl. Phys. Lett.* 113, 222405 (2018).
- [21] S. Yamada, Y. Nishibe, M. Saizaki, H. Kitajima, S. Ohtsubo, A. Morimoto, T. Shimizu, K. Ishida, and Y. Masaki, *Jpn. J. Appl. Phys.* 41, L206 (2002).
- [22] ICSD database, <https://icsd.fiz-karlsruhe.de/index.xhtml>.
- [23] S. Tomiyoshi, Y. Yamaguchi, and T. Nagamiya, *J. Magn. Magn. Mater.* 31–34, 629 (1983).
- [24] J. Noky, J. Goth, C. Felser, and Y. Sun, *Phys. Rev. B* 98, 241106 (R) (2018).
- [25] Jing Zhou, Xiao Wang, Yaohua Liu, Jihang Yu, Huixia Fu, Liang Liu, Shaohai Chen, Jinyu Deng, Weinan Lin, Xinyu Shu, Heng Yau Yoong, Tao Hong, Masaaki Matsuda, Ping Yang, Stefan Adams, Binghai Yan, Xiufeng Han and Jingsheng Chen, *Sci. Adv.* 5, eaau6696 (2019).
- [26] J. Sinova, S.O. Valenzuela, J. Wunderlich, C.H. Back, and T. Jungwirth, *Rev. Mod. Phys.* 87, 1213 (2015).
- [27] H. L. Wang, C. H. Du, Y. Pu, R. Adur, P. C. Hammel, and F. Y. Yang, *Phys. Rev. Lett.* 112, 197201 (2014).
- [28] L. Liu, T. Moriyama, D. C. Palph, and R. A. Buhrman, *Phys. Rev. Lett.* 106, 036601 (2011).
- [29] P. K. Muduli, T. Higo, T. Nishikawa, D. Qu, H. Isshiki, K. Kondou, D. Nishio-Hamane, S. Nakatsuji, and YoshiChika Otani, *Phys. Rev. B* 99, 184425 (2019).